Liu *et al. Energy Mater.* **2025**, *5*, 500024
DOI: 10.20517/energymater.2024.101

Energy Materials

Article

Open Access

Synergistic design and synthesis of O, N Co-doped hierarchical porous carbon for enhanced supercapacitor performance

Hongwei Liu[1,2,3], Zhenming Cui[1,2,3], Yan Sun[1,2,3], Zhennan Qiao[1,2,3], Yanlan Zhang[1,2,3], Qiang Bai[1], Yongzhen Wang[1,2,3,*]

[1]College of Materials Science and Engineering, Taiyuan University of Technology, Taiyuan 030024, Shanxi, China.
[2]Shanxi Joint Laboratory of Coal-based Solid Waste Resource Utilization and Green Development, Taiyuan University of Technology, Taiyuan 030024, Shanxi, China.
[3]Innovation Research Center for Materials Genetic Engineering, Taiyuan University of Technology, Taiyuan 030024, Shanxi, China.

[*]**Correspondence to:** Prof. Yongzhen Wang, College of Materials Science and Engineering, Taiyuan University of Technology, 79 Yingze West Main Street, Taiyuan 030024, Shanxi, China. E-mail: wangyongzhen@tyut.edu.cn

How to cite this article: Liu, H.; Cui, Z.; Sun, Y.; Qiao, Z.; Zhang, Y.; Bai, Q.; Wang, Y. Synergistic design and synthesis of O, N Co-doped hierarchical porous carbon for enhanced supercapacitor performance. *Energy Mater.* **2025**, *5*, 500024. https://dx.doi.org/10.20517/energymater.2024.101

Received: 1 Aug 2024 **First Decision:** 28 Aug 2024 **Revised:** 16 Sep 2024 **Accepted:** 25 Oct 2024 **Published:** 16 Jan 2025

Academic Editor: Wei Tang **Copy Editor:** Ping Zhang **Production Editor:** Ping Zhang

Abstract

Carbon-based supercapacitors have emerged as promising energy storage components for renewable energy applications due to the unique combination of various physicochemical characteristics in porous carbon materials (PCMs) that can improve specific capacitance (SC) properties. It is essential to develop a methodical approach that exploits the synergy of these effects in PCMs to achieve superior capacitance performance. In this study, machine learning (ML) provided a clear direction for experiments in the screening of key physicochemical features; SHapley Additive exPlanations analysis on ML indicated that specific surface area and specific doping species had a significant synergistic impact on SC enhancement. Utilizing these insights, an O, N co-doped hierarchical porous carbon (ONPC-900) was synthesized using a synergistic pyrolysis strategy through K_2CO_3-assisted *in-situ* thermal exfoliation and nanopore generation. This method leverages the role of carbon nitride (graphite-phase carbon nitride) as an *in-situ* layer-stacked template and the oxygen (O)-rich properties of the pre-treated lignite, enabling controlled synthesis of graphene-like folded and amorphous hybrid structures engineered for the efficient N and O doping sites and high specific surface area, resulting in an electrode material with enhanced structural adaptability, rapid charge transfer, and diffusion mass transfer capacity. Density functional theory (DFT) calculations further confirmed that pyrrole nitrogen (N-5), carboxyl (-COOH) active sites, and the defect structure formed by pores

synergically enhanced the adsorption of electrolyte ions (K^+) and electron transfer, improving the SC performance. The optimized ONPC-900 electrode exhibited impressive SC properties of 440 F g^{-1} (0.5 A g^{-1}), outperforming most coal-based PCMs. This study provides a methodology for designing and synthesizing high SC electrode materials by optimizing the key characteristic parameters of synergism from complex structure-activity relationships through the combination of ML screening, experimental synthesis, and density functional theory validation.

Keywords: Synergy, defect, *in-situ* exfoliation, doping active site, machine learning, DFT calculations

INTRODUCTION

Supercapacitors offer promising opportunities for energy storage applications due to their impressive power density, long cycle life, and fast charge/discharge rates[1-3]. However, high-performance supercapacitors are largely dependent on the structural composition and physicochemical characteristics of the electrode materials used. Thus, a critical hurdle in maximizing the potential of supercapacitors is the development design and optimization selection of high-performance electrode materials. Porous carbon materials (PCMs) are carbon-based electrode materials frequently used in supercapacitors to boost their capacitive capabilities owing to their rich pore structure, excellent conductivity, high ion-accessible specific surface area (SSA), and ease of production[4,5]. Previous research has introduced various synthetic strategies for creating porous structures in PCMs, aiming to achieve high SSA and desired pore characteristics[6]. Improving the SSA and optimizing pore structures - including creating sub-nanopore or hierarchical structured pores with micropores, mesopores, and macropores - were considered effective approaches for enhancing the actual specific capacitance (SC) of carbon-based supercapacitors due to the constraints of the adsorption mechanism in electrical double-layer capacitors (EDLCs)[7-9]. Nonetheless, due to the diversity of PCM precursors and the intricate nature of amorphous porous materials, the controlled modulation of morphological microstructure remains a major challenge. Additionally, the inherent synergies of various features such as morphological microstructure, SSA, and pore structure are ignored in the optimization and synthesis of PCMs with high expected performance.

Moreover, the capacitance properties of PCMs can be improved at a higher level by incorporating heteroatoms and adjusting wettability, reactivity, and pseudo-capacitance[10-12]. Lignite, as an O-containing carbon precursor, has gained attention in research because of its wide range of precursor sources, cost-effectiveness, and natural O-doping properties[13,14]. The presence of O-containing functional groups on carbon materials significantly enhances capacitance by introducing redox pseudo-capacitance, improving wettability, and enhancing conductivity[15]. Artificial doping is carried out by using dopants containing nitrogen (N), sulfur (S), boron (B), and other heteroatoms[16-18]. Among these, N-doping into a carbon matrix is considered the most promising approach for enhancing the pseudo-capacitance performance[19-21]. However, N heteroatoms are bound to C as amorphous elements, resulting in low nitrogen content and potential issues such as the failure of functional groups and damage to the structural stability. To solve these problems, the incorporation of graphite-phase carbon nitride (g-C_3N_4) into PCMs is carefully controlled to integrate with the carbon skeleton in a specific manner, potentially forming unique structures where carbon atoms compensate for deficiencies and enhance the energy storage active sites in PCMs[22-25]. Therefore, it is of great significance to select nanostructured heteroatom-rich carbon precursors or template agents rich in heteroatoms to effectively couple the dopant of the hierarchical porous structure and reaction active site, improving structural features for synergistically enhancing the capacitance characteristics of supercapacitors. Although experiments have confirmed the combined physicochemical features including SSA, pore structure, morphology structure, and heteroatom doping of PCMs synergistically improve capacitance performance, effective strategies to fully explain this complex mechanism effect are still

lacking[26], especially when it comes to the synergistic mechanism of certain key physicochemical characteristics on capacitance enhancement. Density functional theory (DFT) was used to investigate how heteroatoms affect equilibrium properties and contribute to the improved capacitance of PCMs. Kolavada *et al.* used DFT calculations to study the interaction between quantum capacitance and electrode materials[27]. Through theoretical calculations of quantum capacitance, researchers can deeply analyze the charge storage capacity of supercapacitor electrodes and provide precise quantum-level predictions of their behavior by using DFT simulations. These calculations are helpful for mechanism interpretation, experimental verification and design optimization of supercapacitors[27,28]. However, the role between the quantum capacitance and the structure of electrode material does not include the correlation between the EDLC and the physicochemical characteristics (total capacitance includes EDLC and quantum capacitance). For this reason, it is still difficult to evaluate some key physicochemical features with quantum capacitance calculations, especially through the synergistic structure-activity relationship involving double-layer capacitance (such as SSA) and quantum capacitance (heteroatom doping) with total capacitance. A novel machine learning (ML) strategy is applied to assist the design of supercapacitor materials with superior performance by excavating the connection between capacitance and significant features of electrode materials[29]. In numerous studies, SHapley Additive explanation (SHAP) with comprehensive interpretability based on ML provides insights for the screening of key characteristics of electrode materials that affect capacitance properties. While various ML models were widely used to explain and predict the performance of materials or devices in electrochemistry, most solely focus on model screening and application and rarely combine them with experiments[30-32]. Moreover, both experimentally and theoretically, the effects of single features have been thoroughly studied, while the impact of multi-feature factors often falls short in synergistic explanations. The combination of ML, experimental methods and DFT allows for quicker screening of key physical and chemical characteristics from a variety of features, and, at the same time, provides experimental and DFT theoretical simulation verification, offering comprehensive guidance and in-depth explanation of mechanism for the optimization and design of new materials.

Herein, we propose an ML-guided key feature screening optimization and interpretable analysis, successfully synthesizing PCMs with superior key features, and a DFT-assisted validation combination method for optimal design of supercapacitor electrode materials with expected performance. To achieve this, SHAP in ML was used to reveal the interaction impacts of characteristics on SC and screen key features that have positive effects on capacitance enhancement. Based on ML interpretability analysis screening of key physicochemical features, we developed a facile *in-situ* exfoliation and pore-forming engineered synergistic pyrolysis strategy for constructing and synthesis the O, N co-doped hierarchical porous carbon (ONPC) materials. Physicochemical characterization and electrochemical kinetic quantitative analysis were used to evaluate the significant effects of SSA and N, O co-doped effective active species (such as N-5, -COOH, *etc.*) on capacitance enhancement. In addition, the adsorption energy of ONPC adsorbed electrolyte (K^+) was calculated using DFT to infer and verify the interaction mechanism between pore defect structure and specific doping species. The as-obtained optimal ONPC-900 exhibits a high SSA (802 $m^2 g^{-1}$), hierarchical porous structure and effective active species (10.13%). Benefiting from the large SSA of the double-layer capacitance contribution and the N, O co-doped pseudo-capacitance contribution, the excellent capacitive performance of ONPC-900 is unveiled and the SC is 440 F g^{-1} (0.5 A g^{-1}). The calculation results of DFT further confirmed that O and N co-doping promoted the increase of SC and revealed that the inner defect co-doped by O and N is significantly more effective than edge co-doping in ONPC materials. Theoretical calculations further confirmed that the synergistic effects of pyrrole nitrogen, carboxyl functional group species and structural defects of pore formation promote the K^+ adsorption and electron transfer, improving the SC performance. This work proposes a straightforward approach that may open a new avenue for designing and synthesizing PCMs based on multiple synergistic effects, while providing a

new paradigm of combined ML, experiment, and DFT-assisted interpretation with comprehensive interpretability.

EXPERIMENTAL

Materials

A typical raw lignite named low-rank coal was collected from the Inner Mongolia Autonomous Region of China. To eliminate the influence of other minerals in the raw lignite, demineralization was carried out using hydrofluoric acid (HF, approximately 20 wt%) and hydrochloric acid (HCl, about 1 M) until the ash content was reduced to less than 1%, resulting in the production of ash-free coal known as pre-treated lignite. The approximate and ultimate analysis results of both raw lignite and pre-treated lignite are presented in Supplementary Table 1. The reagents used included potassium carbonate (K_2CO_3), melamine, sodium hydroxide (NaOH), N, N-dimethylformamide, potassium hydroxide (KOH, ≥ 85%) were purchased from Sinopharm Chemical, polyvinylidene difluoride (PVDF, Shanghai Aladdin Reagent Co., ltd.), N-methylpyrrolidone (NMP), and acetylene black (Shanghai Aladdin Reagent Co., ltd.), all sourced from reputable suppliers without further processing. The deionized water for each experiment is homemade from our laboratory.

Preparation of ONPC materials

ONPC materials were synthesized using the pre-treated lignite and bulk g-C_3N_4 as carbon precursors and heteroatomic dopants. The bulk g-C_3N_4 was synthesized via a previously reported method involving thermal condensation of melamine at 550 °C for 2 h, followed by natural cooling[33]. Subsequently, the bulk g-C_3N_4 was mixed with K_2CO_3 and pre-treated lignite in a 1:1:1 mass ratio, ball milled thoroughly, and pyrolyzed at different temperatures (700 °C, 800 °C, and 900 °C) under a N_2 atmosphere for 3 h. After natural cooling down to room temperature, the reaction product was washed sequentially with an alkali solution and distilled water and finally vacuum dried at 80 °C for 24 h. More specifically, the obtained samples by pyrolysis were ground and placed in 1 M sodium hydroxide solution (mass volume ratio of sample and washing solution: 1 g/10 mL) and washed at 25 °C for 24 h, then centrifuged at 8,000 rpm and purified several times with distilled water until neutral. The final purified sample was obtained by vacuum drying at 80 °C for 24 h after washing. The resulting PCMs were named ONPC-x (x = 700, 800, and 900). For the sake of contrast, the NPC-900 was also obtained at 900 °C pyrolysis by the same procedure and conditions from the pre-treated lignite and g-C_3N_4 as carbon and nitrogen precursors, respectively, without the addition of K_2CO_3. In addition, the synthetic procedure of Oxygen-rich porous carbon (OPC)-900 was similar to that of NPC-900 except for the addition of g-C_3N_4. The synthesized ONPC materials included ONPC-700, ONPC-800, ONPC-900, OPC-900, and NPC-900.

Material characterization

The microstructure and morphology of ONPC samples were investigated using a ZEISS Sigma 300 scanning electron microscope (SEM). Transmission electron microscope (TEM) images and high-resolution TEM (HRTEM) images were acquired on a JEM-F200 (JEOL) TEM coupled with an energy dispersive spectrometer (EDS; JED-2300T). Thermogravimetric curve (TG, NETZSCH, STA449F5) measurement was carried out to study the pyrolysis process of pre-treated lignite, g-C_3N_4, and the mixture precursor after ball milling, respectively. The test conditions are: under Ar protection atmosphere, the heating rate of 10 °C min^{-1}, and the temperature range of 50-1,000 °C. X-ray diffraction (XRD) patterns were obtained by Aeris (Malvern Panalytical, United States) with Cu Kα radiation (λ = 1.5406 Å) to identify the crystal properties of the sample. The SSA, pore size distribution (PSD), and pore textures of all obtained samples were analyzed by an ASAP 2020 PLUS HD88 N_2 adsorption-desorption isotherm analyzer (Micromeritics, USA) at 77 K. The SSA was determined via the Brunauer-Emmett-Teller (BET) method. The PSD curves were derived from the adsorption branch using the nonlocal DFT model. Physicochemical properties and

structure characteristics of the ONPC materials were analyzed by X-ray photoelectron spectroscopy (XPS, Thermo Scientific K-Alpha) and Raman spectra (λ = 532 nm, Horiba LabRAM HR Evolution). Surface composition was characterized by Fourier transforms infrared (FTIR) spectroscopy (Thermo Scientific Nicolet iS20).

Electrochemical measurement and analysis

Electrochemical evaluation was conducted utilizing a standard three or two electrode configurations, with all measurements analyzed using a CHI760E (Shanghai Chenhua). In the three-electrode cell, the Pt plate and Hg/HgO served as the counter and reference electrodes, respectively, in a 6 M KOH aqueous electrolyte solution. Prior to the electrochemical tests, the working electrodes were prepared. The preparation process involved grinding an active material with a mass fraction of 80% along with carbon black (10%) in an agate mortar. This mixture was then stirred with N-methyl pyrrolidone as the solvent and polyvinylidene fluoride (PVDF, 10%) to create a mixed electrode slurry. The prepared mixture was drip-coated evenly onto a carbon cloth (1 cm × 1 cm) and dried overnight in a vacuum oven at 80 °C. The weight of the active material after drying was 1.28 mg (1 cm × 1 cm). The samples underwent testing through cyclic voltammetry (CV), galvanostatic charge-discharge (GCD), and electrochemical impedance spectroscopy (EIS). The electrochemical properties of each PCM were investigated by measuring the CV plots at different scan rates at -1~0 V. GCD was performed in the current density range of 0.5 to 20 A g^{-1} under the same voltage window. EIS plots were obtained in a frequency range of 0.01 kHz to 100 kHz with an applied amplitude of 5 mV, and fitting analysis was conducted using an equivalent circuit diagram. The gravimetric SC (C, F g^{-1}) of a three/two-electrode device is formulated as follows:

$$C = \frac{I\Delta t}{m\Delta V} \tag{1}$$

$$C_s = \frac{2I\Delta t}{m\Delta V} \tag{2}$$

where the I (A), ΔV (V), Δt (s), and m (g) represent discharge current (A), test potential during discharging (V), discharge time (s), and the weight of single electrode active material, respectively.

Two electrodes with identical active mass and electrolyte (6M KOH) were incorporated into a symmetric two-electrode supercapacitor system. The electrochemical properties were measured in the voltage window of 0~1 V. The cycle stability of the device was evaluated using a Landt G340A precision battery test system.

The energy densities (E, Wh kg^{-1}) and power densities (P, W kg^{-1}) were rigorously determined by:

$$E = \frac{1000C_s(\Delta V)^2}{8\times3.6} \tag{3}$$

$$P = \frac{E\times3600}{\Delta t} \tag{4}$$

Machine learning-assisted analysis

Data collection and feature engineering

To elucidate the relationship between SC and porous carbon structural characteristics for designing high-performance supercapacitor materials, a dataset comprising 69 sample sets from published papers on O, N co-doped PCMs for supercapacitors was compiled. Various factors influence supercapacitor performance, but many lack specific data or uniform standards, posing challenges for capacitance prediction. Utilizing a 6 M KOH electrolyte, a three-electrode test system, and 15 features (structural, chemical, and operational) of O, N co-doped PCMs, including SSA, micropore surface area (S_{micro}, m^2 g^{-1}),

total pore and micropore volume (V_t and V_{micro}, $cm^3\ g^{-1}$), carbon (C), nitrogen (N), and oxygen (O) content, as well as various functional group ratios (pyridinic nitrogen, N-6; pyrolytic nitrogen, N-5; graphitic nitrogen, N-Q; OI: carbonyl-O group, C=O; OII: hydroxyl-O/ether-O group, C-OH/C-O-C; OIII: carboxyl-O group, -COOH) and specific features such as potential window (PW, V) and current density (CD, $A\ g^{-1}$), were extracted as predictive features. Subsequently, the dataset was divided into a training set of 62 samples and a test set of seven samples for model evaluation. Detailed descriptions of feature selection and data set creation are provided in Supplementary Materials (Section: sample data collection, Supplementary Figures 1 and 2, Supplementary Table 2).

ML model evaluation and interpretation

Research has demonstrated that Random Forest (RF) modeling is more feasible and efficient than other methods for evaluating feature importance, particularly in high-latitude data. Therefore, the RF model was adopted as the predictive model in this study and trained according to the data collected in the literature. The ML algorithms for the RF models were implemented in a Python programming environment, with the primary ML package being scikit-learn. To begin the analytical process and provide an overview of correlation analysis based on the dataset, all considered feature variables were evaluated using the Pearson correlation coefficient (*PCC*). This coefficient measures linear correlation between feature variables, primarily to assess collinearity and the relationship between the independent (porous structure) and dependent or target (capacitive performance) variables. The reliability of ML models was assessed using various measurement methods, including the *PCC*, Mean Absolute Error (MAE), Root Mean Square Error (RMSE), and R-square (R^2) between the expected and estimated outputs from the ML model. These parameters can be calculated as follows:

$$PCC = \frac{\sum_{i=1}^{n}(x_i-\bar{x})\sum_{i=1}^{n}|y_i-\bar{y}|}{\sqrt{\sum_{i=1}^{n}(x_i-\bar{x})^2}\sqrt{\sum_{i=1}^{n}(y_i-\bar{y})^2}} \quad (5)$$

$$MAE = \frac{1}{n}\sum_{i=1}^{n}|y_i-\hat{y}_i| \quad (6)$$

$$RMSE = \sqrt{\frac{1}{n}\sum_{i=1}^{n}|y_i-\hat{y}_i|^2} \quad (7)$$

$$R^2 = \frac{\sum_i(\hat{y}_i-y_i)^2}{\sum_i(y_i-\bar{y})^2} \quad (8)$$

where n represents the number of samples, y_i is the real capacitance, $\bar{y}$ is the mean value of the real capacitances and $\hat{y}_i$ is a predicted value of the ML model. SHAP was generated based on the preferred model to explain the influence of each feature on SC. This approach, rooted in game theory, aims to explain the output of any ML model. The SHAP values represent the marginal contributions of the 12 features to the SC output. Through quantitative analysis using SHAP values, the total impact of multiple features on the output can be investigated. This method recommends optimized feature parameters for high-performance O, N co-doped PCMs and explains the complex mechanism effects of key features on enhancing the SC of O, N co-doped PCMs.

DFT calculations

The heteroatomic doping structure of the electrode material was optimized utilizing DFT calculations with the Vienna Ab initio Simulation Package (VASP)[34]. The calculations employed a plane wave base set with an energy cutoff of 600 eV, a projected-enhanced wave pseudo-potential, and a generalized gradient approximation of the exchange-correlation functional parameterized by Perdew, Burke, and Ernzerhof. The model structure underwent full optimization for ionic and electronic degrees of freedom, with electronic energy convergence criteria set at 10^{-5} eV and force convergence criteria at 10^{-2} eV/Å for each atom. The

absorbed electrolyte energy (E_a) of the electrolyte ion (K^+) on an undoped or doped carbon surface is defined by:

$$E_a = E_{total} - E_{surf} - E_K \quad (9)$$

where E_{total} represents the total energy after electrolyte ion adsorption, E_{surf} is the undoped or doped carbon surface energy, and E_{K+} is the energy of a single K^+ in the bulk position.

RESULTS AND DISCUSSION

Considering the advantages of ML, which can reduce experimental and computational costs and accelerate the discovery and optimization of new materials, we chose the influence of multi-physicochemical characteristic parameters on the SC performance of supercapacitor electrode materials as the research point. By gathering existing literature data and building a ML model, combined with comprehensive interpretability analysis (SHAP analysis), critical and positively correlated features can be extracted or selected to accelerate the design and synthesis of new materials. ML-assisted analysis using literature datasets was employed to reveal the multiple roles of various physicochemical features on enhancing the SC properties of ONPC materials. Deeper insights into the structure-activity relationship of ONPC materials were obtained by assessing the impacts of different features on each other and on the output variable. A *PCC* matrix was utilized to provide an overview of the correlation analysis among variables in the dataset. Some physicochemical characteristics of ONPC materials exhibited weak correlations with SC ($r < 0.3$) in the *PCC* matrix [Figure 1A], suggesting that the relationship between these specific characteristics and capacitive performance cannot be adequately explained by a linear function. This also indicates that there exists an interdependence among different physicochemical attributes for enhancing SC. A subset of 12 features (excluding strongly correlated variables such as S_{mic}, V_{mic}, and V_t from the original 15 feature values) showing high correlation with pore structure features and capacitance were selected for modeling. The optimized ML model highlighted in Supplementary Figure 3 shows the RF model prediction outcomes (R^2 = 0.86, RMSE = 17.11, and MAE = 12.78). Additionally, RF has considered the impact of all features comprehensively, as illustrated by the SHAP waterfall diagram of the model. The importance of 12 features was ranked through SHAP analysis [Figure 1B], highlighting the marginal contribution of each feature to the output using SHAP values. Figure 1B revealed that these parameters, such as SSA, N-Q%, N%, C=O%, -COOH%, C-OH/C-O-C%, N-5%, and O%, have significant impacts on SC, aligning with findings from previous literature[30,32,35]. The positive influences of SSA, -COOH%, N-5%, O%, and N-6% in physicochemical features were also confirmed by SHAP analysis. The ambiguous evaluation of N% in Figure 1B is due to the complexity of N-doping content, doping form, and types of N-containing functional groups, leading to uncertainty regarding its overall impact on capacitor performance. The analysis demonstrated that increasing the O-doping content has a limited impact on improving capacitance, as shown in Figure 1B where low SHAP values indicate a positive effect. Moderate O-doping could enhance SC by enhancing conductivity and improving electrode wettability. Moreover, the presence of carboxyl-O (-COOH) in alkaline electrolyte acts as an effective active site, contributing to additional pseudo-capacitance, while carbonyl-O has a negative effect due to inappropriate O-doping functional groups at the skeleton edges of carbon causing steric hindrance[36]. This can obstruct the porosity characteristics of the carbon material and reduce capacitive electrochemical performance. Furthermore, feature clustering analysis was utilized to assess the relative importance of these features [Figure 1C]. Notably, the RF model prioritized structural parameters such as "SSA", "N-Q", "N", and "C=O". Combined with the analysis of Figure 1B and C, it is revealed that a 57.2% improvement in capacitance was achieved by increasing SSA, reducing N-Q proportion, elevating N content, and regulating C=O distribution. This observation supports our ONPC materials design considerations that the structure engineering of pore and

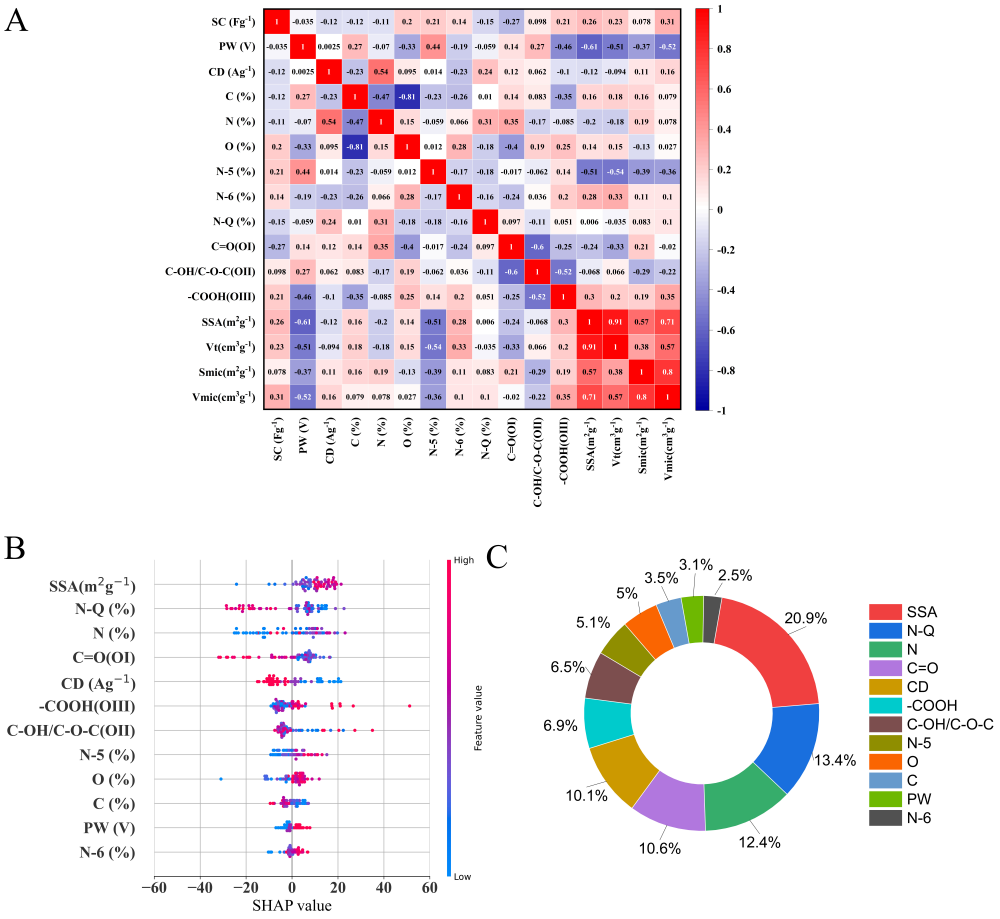

Figure 1. ML-assisted Analytics. (A) Heatmap of between features and SC (The colors of squares in the heat map represent the correlation's strength and direction); (B) SHAP waterfall diagram of feature importance; (C) Marginal contribution of twelve input features to the output variables based on a RF model. ML: Machine learning; SC: Specific capacitance; SHAP: SHapley Additive explanation; RF: Random forest.

doping drastically boosted SC peculiarity, promoting excellent performance through the synergistic effects of the optimization of positive feature factors and the weakening of negative factors interactions. In other words, enhancing capacitive performance involves a combination of factors such as increasing the SSA, optimizing N or O content, moderating N-Q, and promoting the formation of carboxyl-O and N-5 active sites.

Through ML-assisted interpretability analysis to optimize key features and rational design aided by in-situ catalytic pyrolysis, we successfully synthesized an ONPC material engineered for the efficient N and O doping sites, high SSA and utilization of graphene-like folding and amorphous hybrid. The process of synthesizing ONPC materials was depicted in Figure 2A. Essentially, ONPC materials were prepared using pre-treated lignite as a carbon precursor and oxygen source, g-C_3N_4 as a template, carbon precursors, and nitrogen source. This synthesis involves a straightforward ball-milling process and high-temperature pyrolysis, with the addition of K_2CO_3. The addition of K_2CO_3 serves a dual purpose: facilitating the high-temperature *in-situ* exfoliation of bulk g-C_3N_4 to form graphene-like structures while catalyzing the pyrolysis of oxygen-rich pre-treated lignite to produce pore structures and retain oxygen-rich properties. In this synthesis, ONPC carbon material, pre-treated lignite and g-C_3N_4 work together to form the carbon

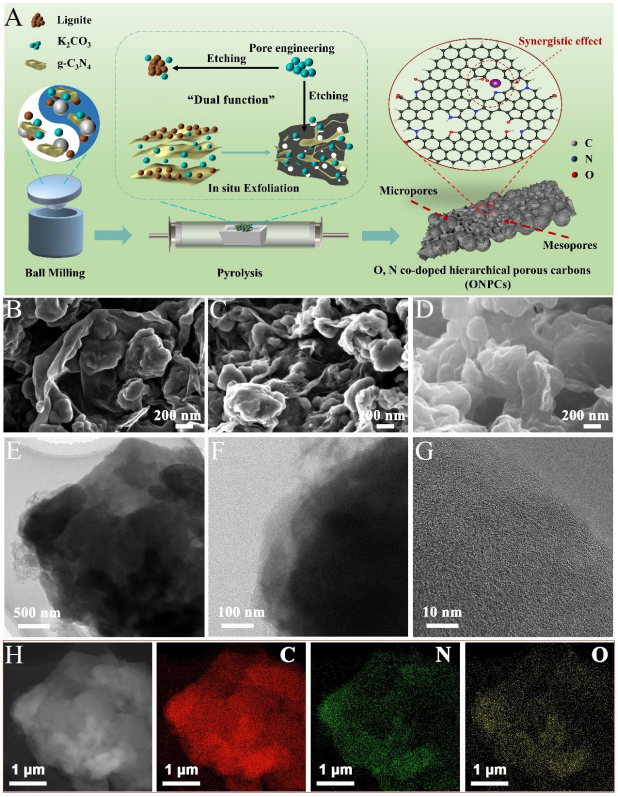

Figure 2. (A) Schematic illustration of synergistic fabricated ONPC materials; (B-D) SEM images of ONPC-700, ONPC-800, and ONPC-900, respectively. TEM images of ONPC-900; (D) low resolution; (E-G) high resolution, and (H) element mapping of C, N, and O. ONPC: O, N co-doped hierarchical porous carbon; SEM: Scanning electron microscope; TEM: Transmission electron microscope.

skeleton of ONPC, which, together with K_2CO_3, form the core of our collaborative *in-situ* pyrolysis reaction. We utilized the K_2CO_3 assisted pyrolysis strategy and verified it experimentally to ensure synergistic synthesis. Also, control samples (pre-treated lignite, bulk g-C_3N_4, OPC-900 and NPC-900) were prepared with some changes (details are given in "Experimental sections"). The OPC-900 material exhibited similar irregular spheroidal structures [Supplementary Figure 4A], indicating that it retained the morphological structure of pre-treated lignite. The NPC-900 material [Supplementary Figure 4B] revealed lamellar structures within irregular lignite-derived carbon structures, indicating that g-C_3N_4 served as a structural template agent, altering the structure of the synthesized carbon material. Upon the introduction of K_2CO_3, all ONPC materials displayed irregular spheroidal morphology enveloped by graphene-like folds [Figure 2B-D], highlighting the thermal exfoliation effect of K_2CO_3 during high-temperature pyrolysis. The ONPC-900 displayed a hybrid carbon structure with fewer graphene-like folded layers while still maintaining the spheroidal amorphous carbon structure inherited from the pre-treated lignite, significantly enhancing SSA and V_t compared to ONPC precursors [Figure 2D-F, Supplementary Figures 4-6, and Supplementary Table3]. During synthesis, the pre-treated lignite acted as an oxygen-doped carbon precursor; bulk g-C_3N_4 served as an *in-situ* template and was subsequently stripped and etched by K-containing species released by the decomposition of K_2CO_3 [Supplementary Figure 7], optimizing the morphology of ONPC, increasing the accessibility of N, O co-doping active sites, and facilitating the transformation of bulk g-C_3N_4 into a graphene-like fold structure. TEM images of ONPC-900 further confirmed the presence of graphene-like fold nanosheets derived from the template agent g-C_3N_4 on the surface of amorphous carbon spheroid structure originating from pre-treated lignite [Figure 2E]. Distinct graphene-like folds attached to the surface of lignite-derived amorphous carbon were observed at high

magnification [Figure 2F]. These folds are attributed to the catalytic activation of pre-treated lignite and the high-temperature thermal exfoliation of g-C_3N_4 by K_2CO_3 during pyrolysis. The resultant ONPC-900 presented randomly orientated graphitic carbon uniformly doped with N and O elements [Figure 2G-H], mirroring the graphene-like folding and amorphous hybrid. These observations underscore the key role of K_2CO_3 in modulating the synthesis of N, O co-doped porous carbon with a balanced coexistence of graphitized and amorphous carbon structure, regulating the kinetics equilibrium of heteroatom doped precursors in the pyrolysis process, and promoting N and O co-doping.

Subsequent analysis of nitrogen adsorption-desorption curves provided insight into the microscopic pore structure of the ONPC materials. It is important to highlight that the deliberately designed K_2CO_3 played a significant role in regulating the pore structure and balancing the amorphous and graphitized hybrid structure of the PCMs, thereby enhancing its energy storage capabilities. The isothermal adsorption/desorption curves of ONPC materials demonstrated a combination of type I and IV characteristics in Figure 3A, indicating the existence of micro and mesoporous. The PSD from 0.4 nm to 4 nm [Figure 3B] further confirmed the hierarchical pore structure of the ONPC materials, with micropores being predominant and small mesopores coexisting. A comparative analysis of micropore surface area, mesopore surface area, and micropore volume ratio (V_{mic}/V_t) was presented in Figure 3C. The comparison of OPC-900, NPC-900 and ONPC-900 revealed the equilibrium effect of K_2CO_3 in the process of g-C_3N_4 stripping and etching pre-treatment lignite. The comparison of ONPC-900 with ONPC-700 and ONPC-800 shows the rapid increase of micro and mesoporous surface area and the proportion of microporosity, which confirms that temperature changes significantly affect the balance of carbon stripping, nitriding of potassium carbonate, and etching pre-treatment of lignite. Meanwhile, the lower SSA (14 $m^2 g^{-1}$) and V_t (0.01 $cm^3 \cdot g^{-1}$) of ONPC-700 can be linked to the incomplete thermal exfoliation of g-C_3N_4 by K_2CO_3 at 700 ℃, resulting in the formation of multilayer graphene-like folds stacked on the surface of the pre-treated lignite-derived carbon, thereby reducing SSA and pore volume. The distribution ratio of micropores (< 2 nm) in all samples was notably high, while mesopore pore volumes were relatively low, except for the ONPC-700. These results of SSA and microporosity indicate that a lower pyrolysis temperature is more favorable to the *in-situ* thermal exfoliation of K_2CO_3. Higher temperatures facilitate etching of K_2CO_3 to create pores. The detailed parameters of pore structure characteristics, including SSA, pore volume, average pore diameter (D_{ave}), and the percentage of micropore volume, were presented in Supplementary Table 4. ONPC-900 materials showed a dominant pore structure with a total SSA of 802 $m^2 g^{-1}$, a total pore volume (V_t) of 0.37 $cm^3 \cdot g^{-1}$, a micropore volume ratio of 92%, and an average pore size of 1.84 nm, distinguishing it from other ONPC materials. Notably, micropores can serve as active ion sites for electrolyte adsorption, while mesopores are crucial for facilitating ion transfer. These findings demonstrate that the introduction of K_2CO_3 indeed regulates the formation of larger SSA and hierarchical porous structure. It may be inferred that the high SSA, unique hierarchical pore structure, and template-inherited graphene-like fold structure observed in ONPC-900 result from the synergistic equilibrium effect of *in-situ* thermal exfoliation and pore engineering strategies by K_2CO_3 during the formation process.

The carbonization transition of g-C_3N_4 by *in-situ* thermal exfoliation coincided with the emergence of by-product potassium cyanide [Supplementary Figure 8A], characterized by the reduction of triazine units and changes of vibration modes [Figure 4A][37]. All purified ONPC materials [Supplementary Figure 8B] showed double characteristic peaks that can be derived from the graphitization transition of g-C_3N_4 and the carbonization amorphous form of pre-treated[38]. The K content of the ONPC-900 sample is almost 0.16%, revealed by inductively coupled plasma emission spectroscopy (ICP-OES), revealing the complete removal of K-containing by-products, which side confirmed the purity of the ONPC-900 purified sample.

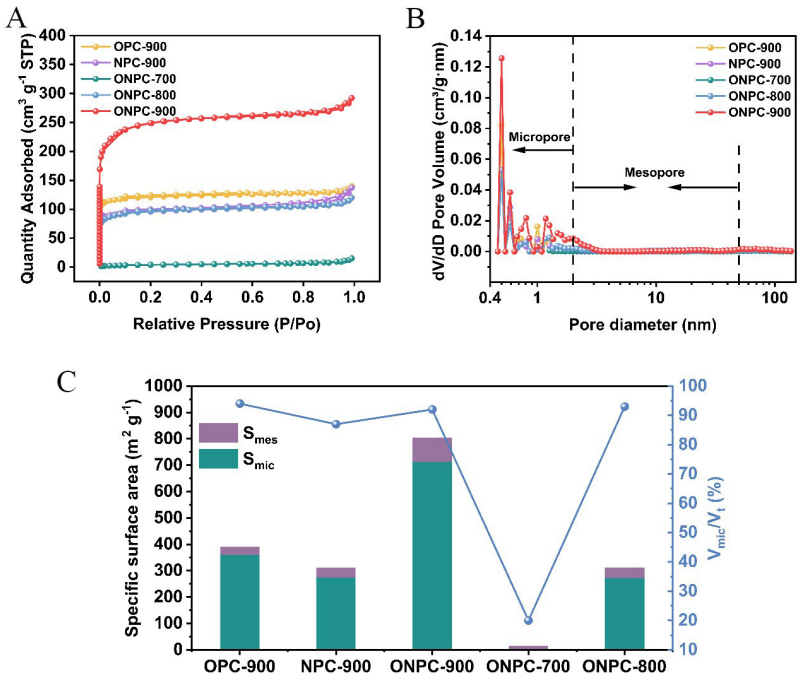

Figure 3. Pore structural characteristics of ONPC materials. (A) Nitrogen adsorption-desorption curves; (B) Pore-size distribution; (C) Specific surface area of mesopore and micropore and micropore volume ratio (V_{mic}/V_t). ONPC: O, N co-doped hierarchical porous carbon.

Additionally, the high-slope curve in the low-angle area of purified ONPC materials in Supplementary Figure 8B suggested that there are numerous micropores, consistent with the results of Figure 3B. Raman spectroscopy revealed two prominent peaks around 1,340 cm^{-1} and 1,593 cm^{-1} [Figure 4B], respectively, corresponding to the D band and the G band, respectively[39]. The D-band and G-band intensity ratio (I_D/I_G) of ONPC-900, standing at 1.18, surpassed those of OPC-900 (1.02) and NPC-900 (1.13), indicating that more defects and pores formation are caused by N and O co-doping into the ONPC-900 framework. The I_D/I_G values were 1.39, 1.42, and 1.18 for ONPC-700, ONPC-800, and ONPC-900, respectively. The decreased disorder degree or higher graphitization in ONPC-900 compared to ONPC-700 and ONPC-800 is due to the synergistic balancing of *in-situ* exfoliation for graphene-like fold layer and *in-situ* etching of pores-forming with the introduction of K_2CO_3 during the pyrolysis process at varying temperatures. The broad 2D peak in materials other than OPC-900 indicates the presence of multilayer graphene layers, likely due to the introduction of g-C_3N_4. The central shift (from 1,585 cm^{-1} to 1,598 cm^{-1}) in the G-band moves in the direction of high displacement in ONPC-700, ONPC-800, and ONPC-900 materials [Supplementary Figure 9], indicating a reduction in the number of graphene layers, which further evidenced the exfoliation effect of K_2CO_3. The full XPS survey shown in Figure 4C confirms the introduction elements of N and the inheritance of O in the ONPC materials. Carbon bonding patterns and N or O doping species were further confirmed by fitting spectra of C, N, and O [Figure 4D-F], respectively. The emerging C-N bond in other samples compared to OPC-900 [Figure 4D] confirms the successful doping of N after adding g-C_3N_4[40]. The N 1s spectrum of OPC-900 in Figure 4E indicates N content below the detection limit, echoing the proximate and ultimate analysis [Supplementary Table 1], reflecting the low nitrogen characteristics of pre-treated lignite. Others displayed the fitting peaks of N-6, N-5, and N-Q species[41], indicating the carbonization phase transformation of g-C_3N_4 structure and increased N-doped functional groups formation. Moreover, the fitted spectral diagram of O 1s in Figure 4F further highlighted the origin of O-containing species, including C=O, C-OH/C-O-C, and -COOH, confirming the successful self-doping of

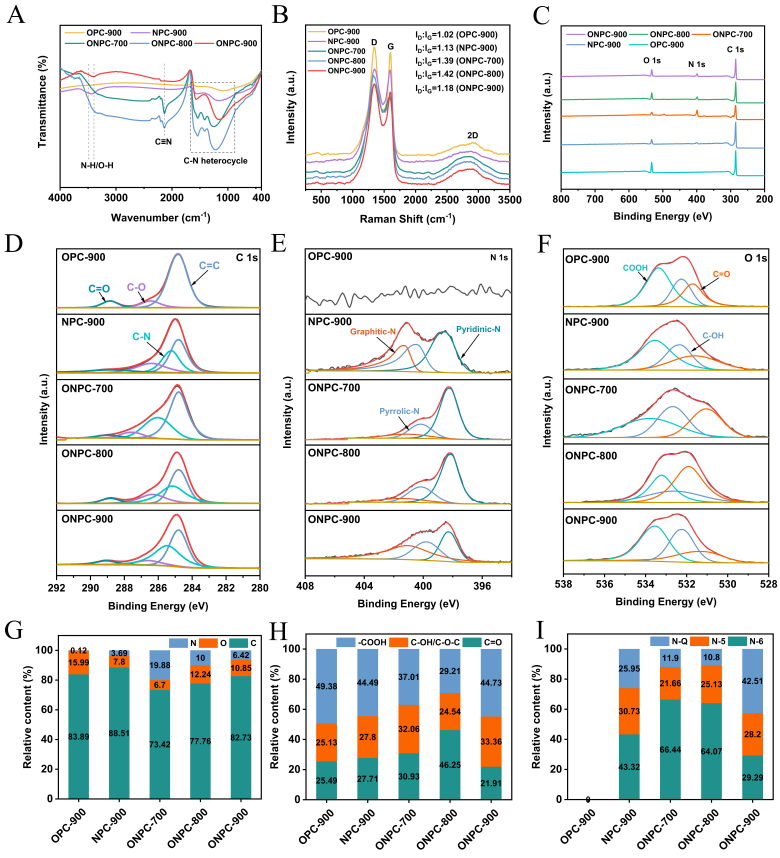

Figure 4. Composition and surface analysis of ONPC materials. (A) FTIR spectra; (B) Raman spectra; (C) Full XPS survey; High-resolution XPS spectra of (D) C 1s, (E) N 1s, and (F) O1s; (G) Relative content of C, N, and O; (H) Relative content of O species; (I) Relative content of N species. ONPC: O, N co-doped hierarchical porous carbon; FTIR: Fourier transforms infrared; XPS: X-ray photoelectron spectroscopy.

O and the inheritance of O species. In Figure 4G, the OPC-900 exhibited the lowest N content (0.12 at%) and the highest O content (15.99 at%), reflecting the high O and low N characteristics inherited from pre-treated lignite. It is further confirmed that the introduction of g-C_3N_4 as a nitrogen dopant leads to oxygen loss, and the addition of K_2CO_3 may facilitate the N, O co-doping into the carbon skeleton. The decrease in N content in ONPC-700, ONPC-800, and ONPC-900 is attributed to a decrease in the number of graphene-like folded layers, as confirmed by the Raman spectra [Supplementary Figure 9]. Figure 4H and I summarized the O 1s and N 1s relative percentages of functional groups. The ONPC-900 showed relatively high contents of C-OH/C-O-C and -COOH [Figure 4H], and N-6 and N-5 relatively content reaching up to 28.2 % and 42.51 % [Figure 4I], surpassing those of ONPC-700 and ONPC-800. These findings highlight the balancing regulatory role of K_2CO_3 in the synthesis of ONPC materials. The change of nitrogen species content of ONPC-900 further confirmed the conversion of N-6 and N-5 to N-Q with the increase of pyrolysis temperature. It is regarded that N-6 and N-5 atoms at the graphitic layer edge create defects and furnish electrically active sites, enhancing pseudo-capacitance for potassium ion (K^+) storage, while N-Q atoms inside the graphitic carbon plane improve conductivity. Oxygen functionalities enhance the wettability of the material, reduce the mass transfer resistance, and participate in redox reactions with the alkaline electrolyte during charge and discharge processes, thereby imparting additional pseudo-capacitance to the PCMs. Therefore, the N and O content of active functional components, acquired by the integral areas of the deconvoluted N 1 s and O 1 s peaks, as listed in Supplementary Table 5, was used to analyze the

total active site of the ONPC materials. The total content of N-5/-COOH/C-O-C or C-OH in ONPC-900 is notably higher at 10.13 at%, which is superior to that of the ONPC-700 (10.0 at%), ONPC-800 (8.78 at%), and NPC-900 (6.71 at%). It is worth noting that pyrrole-N/alcohols/epoxies/carboxy-O can serve as active sites to further provide additional pseudo-capacitors in alkaline electrolytes. ONPC-900 exhibited a relatively high content of N-Q (at%) in Supplementary Table 5, which could enhance conductivity and reduce mass transfer resistance. Moreover, oxygen-rich functional groups present in ONPC-900 are advantageous for improving surface wettability, promoting ion diffusion, and maximizing their electrochemical activity. The presence of these active species underscores the regulatory role of K_2CO_3 during synthesis, ensuring the activity of the synthesized ONPC material as electrode materials. Based on the above structural characterization analysis, we successfully synthesized ONPC materials with the key physical and chemical advantages revealed by ML.

Driven by the hierarchical porous structures with a high SSA, significant pore volume, and abundant active species such as N-5 and -COOH, along with a sub-nanopore dominated, interconnected graphene-like fold layered on pre-treated lignite derived carbon backbones, ONPC-900 exhibited superior electrochemical performance for supercapacitor. CV plots of obtained ONPC materials exhibited distorted quasi-rectangular shapes with obvious pseudocapacitive peaks [Figure 5A and Supplementary Figure 10], while the GCD curves displayed linear shapes with slight deviations [Figure 5B and Supplementary Figure 11], indicating a combination of EDLC and pseudocapacitive behaviors. Furthermore, significant deformation in the CV curves at high scanning rates suggests limitations in the sub-nanopore structure and ion diffusion, leading to uncompensated resistance. Additionally, the asymmetry in the GCD curves may be attributed to the presence of N and O heteroatoms. We noticed that some electrodes such as OPC-900 in Figure 5C exhibit higher discharge time over charge time, which may be due to the redox reaction of functional groups doped with O and N heteroatoms at low potential under low CD (0.5 A g^{-1}). Other reasons may be attributed to the high oxygen doping content (XPS: O, 15.99%) and high micropore ratio (94%) in the OPC-900 sample (BET analysis), a large number of oxygen functional groups may form steric hindrance in the pore structure, resulting in a tail, making the discharge time greater than the charge time. Fascinatingly, we observed the coulombic efficiency (CE) of OPC-900 electrodes at 5 A g^{-1} is about 107.65% and 104.84% at the 1st GCD cycle and after the 10000th GCD cycle, respectively [Supplementary Figure 12A]. The CE variation of the OPC-900 electrode with the GCD cycle can be observed in Supplementary Figure 12B. For carbon electrodes, it is relatively rare to obtain consistently high CE over 1000 GCD cycles. Further, taking the OPC-900 electrode as an example, the CE of the OPC-900 electrode at different current densities was tested through 500 cycles after equipment calibration, and the results showed that the CE of the OPC-900 was still above 100% at different CDs (A g^{-1}) after 500 cycles [Supplementary Figure 12C]. These may originate from the fact that the interaction of electrode materials and electrolytes in supercapacitors can lead to side reactions, such as parasitic electrochemical reactions that occur during charge transfer, which can increase the CE to more than 100%. However, we did not find any significant redox features in either CV or GCD plots [Supplementary Figures 10A and 11A]. These findings conclude that the higher CE is not due to any phase transition or aging of the electrode, but rather that, as described by Raha *et al.*, "this pseudo-capacitance contribution appears to comes from the parasitic electrochemical charge transfer process during discharge, which is key to achieving ultra-high CE"[42]. Compared to control samples such as OPC-900, NPC-900, ONPC-700, and ONPC-800, ONPC-900 displayed the longest discharge time and the largest enclosed area, characterized by the GCD and CV curves, respectively [Figure 5C and D], meaning the largest SC. This may be attributed to the synergy between the adsorption of large SSA, sub-nanopore and active N and O species. The SC of the ONPC materials as electrodes correlated strongly with the current density. GCD comparison of ONPC materials measured at different current densities further disclosed significant SC capability of ONPC, with ONPC-900 exhibiting the highest observed SC of 440 F g^{-1}, significantly surpassing that of OPC-900, NPC-900, ONPC-

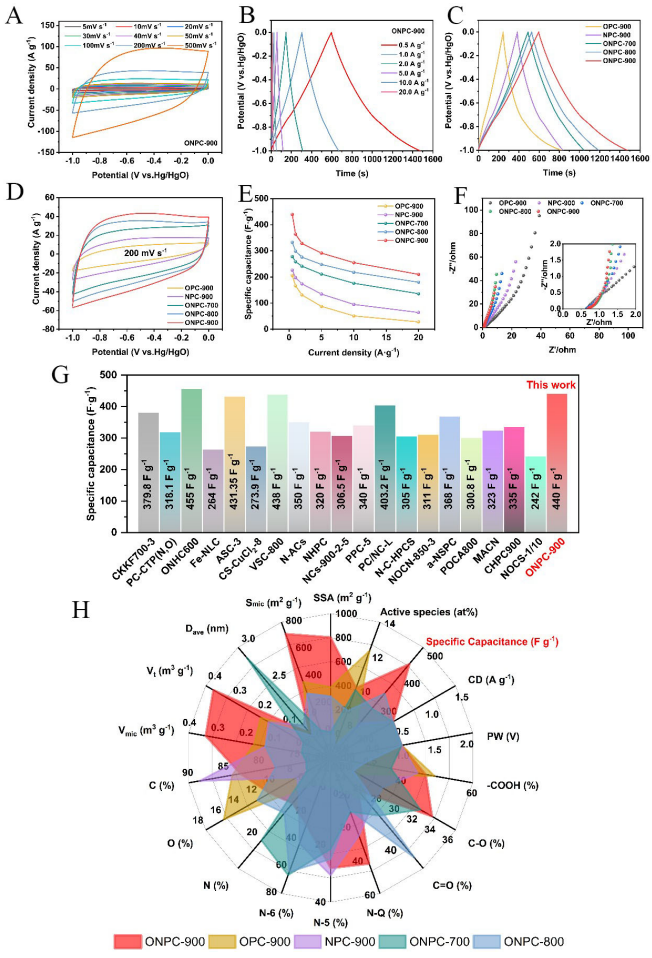

Figure 5. Electrochemical properties of ONPC materials in a three-electrode configuration. (A) CV plots of ONPC-900 measured at various scans (5-500 mV s^{-1}); (B) GCD curves of ONPC-900 measured at various current densities; (C) GCD profiles of ONPC materials; (D) CV curves of ONPC materials; (E) SC comparison of ONPC materials measured at different current densities; (F) Nyquist plots of ONPC materials, inside is the zoomed high-frequency region of ONPC materials; (G) Comparison of the SC with these reported coal-derived carbon materials or ONPC materials[41,44-61]; (H) Radar chart for comparison of seventeen structural and test features and SC (F g^{-1}) of all ONPC materials based on experiment in this work. In particular, the high grades in D_{ave} (average pore diameter) mean low values. ONPC: O, N co-doped hierarchical porous carbon; CV: Cyclic voltammetry; GCD: Galvanostatic charge-discharge.

700, and ONPC-800 by 206, 226, 278, and 333, respectively [Figure 5E]. Low SC values for both OPC-900 (15.99 at% O-doping) and ONPC-700 (19.88 at% N-doping) indicate that excessive O- or N-doping may not be beneficial to the enhancement of SC. Such notable disparity in reactivity also underscores the critical role of K_2CO_3 in regulating and balancing N and O co-doping. The superior SC characteristics of ONPC-900 were due to a combination of these factors. These include a large SSA and pore volume, a relatively concentrated pore diameter with a micro-mesoporous distribution, a balanced amount of O and N co-doping, a high proportion of N and O functional group active species, and few layers of graphene-like fold structure with amorphous carbon. The ONPC-900 electrode maintained a high SC of 210 F g^{-1} even at 20 A g^{-1}, indicating excellent high-rate capability. This may be related to the effect of nitrogen-doped N-Q species. To further analyze the charge/discharge dynamics and to better understand the contribution of the active SSA and O/N heteroatoms to the capacitance, in Supplementary Figure 13, we present the total capacitance (C_t) of electrochemical and the square root of the discharge time. Typically, C comprises EDLC (C_{EDLC}) and pseudo-capacitance (C_P), which are induced by electrostatic adsorption and O/N heteroatomic redox reaction, respectively. Furthermore, according to $C_t = k_1 + k_2 t^{1/2}$[43], C_t is composed of a

rate-independent component k_1 (generally ascribed to C_{EDLC}, the intercept of vertical axis) and a $k_2t^{1/2}$ (related to C_P, the redox reaction induced by heteroatoms, where t is the discharge time) limited by diffusion. The C_t values of ONPC electrodes, as well as the respective contributions from EDLC (C_{EDLC}) and pseudo-capacitance (C_P), were listed in Supplementary Table 6. C_E was lower than 250 F g^{-1} across all samples, which conforms to the limited EDLC in carbon supercapacitors. Therefore, adding highly faradaic-active N, O atoms into the carbon electrodes can significantly improve the SC of the carbon electrode by providing additional C_P, which is also confirmed by the C_P results in Supplementary Table 6. Across all samples, the OPC-900 exhibited the smallest C_t and C_P values, which are greater than C_E, which may be attributed to excessive oxygen doping (15.99%). In contrast, NPC-900 also showed a low C_P value, which may be attributed to low active species contents (6.71%). Based on the mechanism of EDLC energy storage, C_{EDLC} is positively correlated to the effective S_t of ONPC. The contribution value of S_{mic} and S_{mes} of ONPC-900 to the C_t is 241 F g^{-1}, higher than that of ONPC-700 (210 F g^{-1}), ONPC-700 (228 F g^{-1}), OPC-900 (84 F g^{-1}), and NPC-900 (134 F g^{-1}). In addition, ONPC-900 with high N, O co-doping level (O: 10.85%, N: 6.42%, active species:10.13%) provides a C_t of 45.2% (C_P, 199 F g^{-1}). C_t, C_E and C_P values of ONPC-900 were higher than those of ONPC-700 and ONPC-800, which may be due to the synergistic effect of maximum SSA (802 m^2 g^{-1}) and active species (10.13%). The results also revealed the pore structure regulation and stripping effect of K_2CO_3 (reduction of graphene-like fold layer). Excluding control samples OPC-900 and NPC-900, linear fitting of C_E with S_t, S_{mic} and S_{mes} was performed to further explore the effects of S_t, S_{mic} and S_{mes} on C_E of ONPC electrodes, as shown in Supplementary Figure 14. The fitting results of C_E with S_t (R_2 = 0.89243) and S_{mic} (R_2 = 0.89586) were better than that of C_E with S_{mes} (R_2 = 0.85908), revealing the dominant contribution of S_t and S_{mic} to the C_E. Large SSA provides the electrolyte storage facilities. The micropore provides an effective ion adsorption site and mesopore provide a rapid transfer path for the electrolyte, which cooperatively enhance the C_E of ONPC electrodes. EIS plots were further used to analyze the kinetics effects of all ONPC samples. As shown in Figure 5F, all curves show semicircles, oblique lines and nearly vertical lines in different frequency regions. Inside was the zoomed high-frequency region of the Nyquist plots of ONPC materials in Figure 5F. The intercept at the real axis in the zoomed Nyquist plots is the internal resistance (Rs) of ONPC materials, and clearly, the Rs of OPC-900 is lower than that of NPC-900 and ONPC-900, indicating that indicating that the addition of N on the basis of O-doping may change the conductivity of the material. In addition, the Rs values of ONPC-700, ONPC-800, and ONPC-900 are less than that of NPC-900, indicating that the regulation effect of K_2CO_3 is beneficial to the improvement of conductivity. Combining this finding with XPS analysis [Supplementary Table 5] revealed that the negative correlation between Rs and the change of the N-Q true content, which confirmed that N-Q has a significant effect on improving the material conductivity[22]. In addition, XPS and Raman results exhibit that the defects in ONPC materials increase with the introduction of nitrogen, while the Rs changes in ONPC materials are opposite, which is due to the greater contribution of N-Q to the conductivity than the graphite-like carbon with sp^2 hybridization. The charge transfer resistance (R_{ct}) of N-doped carbon materials (except for the OPC-900), related to the semicircle diameter of the impedance curve, all showed a certain pattern. With the N-doping or introduction of N containing functional group, R_{ct} increased gradually and with the content N-6 and N-5 was a positive correlation, which confirms the correlation between Rct and surface pseudo capacitance. The maximum R_{ct} of OPC-900 indicates that excessive O-doping may not be conducive to enhanced charge transfer. ONPC-900 displayed the shortest 45° diagonal line in the mid-frequency region related to ion diffusion resistance (R_w), due to its well-developed pore structure and few-layer graphene-like fold that can provide fast ion transport channels. The low-frequency data region of ONPC-900 displayed a straight line, confirming ultrafine ion diffusion within the electrode. The fitted impedance curves of all ONPC materials are shown in Supplementary Figure 15A, with the equivalent circuit diagram of impedance displayed in the inset. Supplementary Figure 15B presents the magnification of the fitted EIS plots in the high-frequency region for all ONPC materials. The resistance values were listed in Supplementary Table 7. The ONPC-900 exhibited the smallest semicircle and lowest R_{ct} of 0.03 Ω, suggesting rapid ions diffusion

and charge transfer kinetics due to its unique structural features. The low Rs value (0.68 Ω) indicated high electrode conductivity, attributed to the N-Q content and enhanced order graphitized low-layer graphene-like fold structure in the ONPC-900. The Bode diagram [Supplementary Figure 16] shows that the phase angle of ONPC-900 is approximately 76°, which is higher than other materials and closest to 90° (the phase angle of capacitance). The response time τ_0 of ONPC-900 is 1.67 s ($\tau_0 = 1/f_0$, f_0 corresponds to the frequency of the -45° phase Angle), which is lower than OPC-900 (1.83 s), confirming the ability of fast ion transmission and diffusion on the electrode surface after N, O co-doping. The response time τ_0 of other N, O co-doped materials is smaller than ONPC-900, which may be due to the total energy barrier of ion transport and diffusion exerted by the interaction between the pore structure and the species on the pore surface. In other words, the pore architecture and surface N or O species jointly affect the transport and diffusion of ions. Taking everything into consideration, ONPC-900 stands out owing to its largest SSA and active site retention, good pore structure, reasonable N and O doping amount, highest SC, and its low Rs, R_{ct} and R_w. Comparative analysis in Figure 5G also demonstrated that the SC properties of ONPC-900 surpass those of previously reported coal-derived PCMs and O, N co-doped PCMs[41,44-61]. The Radar chart [Figure 5H] derived from the thorough experimental characterization and analysis results illustrates various factors and their corresponding SC. It was observed that ONPC-900 exhibited the highest SC, attributed to the synergistic effects of these multiple feature factors. This comparative result highlights the advantages of our electrode material design, whereby the synergistic optimization of regulatory engineering greatly improves the activity of the ONPC material, thus promoting excellent performance through the synergistic effect of the interaction of pore structure and specific N, O co-doped species active sites. The characterization results and the successful preparation of high-performance ONPC-900 also verified the rationality of the physical-chemical characteristic variables selected by ML.

Based on the analysis of physicochemical features and electrochemical dynamics of the three-electrode system, it appears that active species of N, O co-doped have significant effects on the increase of total SC. Therefore, the theoretical analysis of independent adsorption species was carried out. Given the notable obvious differences in electrolyte affinity and the difficulty of K^+ adsorption, all N-containing or O-containing species of the prepared ONPC materials (based on XPS analysis results) were selected as adsorption sites. The results revealed that the adsorption energy on the surface of undoped carbon was only -27.01 kJ mol^{-1} [Figure 6A]. However, DFT calculations showed large differences in the adsorption energy of K^+ and modulation in the adsorption position on the surface of O-doped or N-doped species [Figure 6B-G]. Doped carbon surfaces with O atoms (C=O/COOH) and N atoms (N-5) exhibited significantly enhanced K^+ adsorption capacities. Notably, the C=O (Figure 6B, E_a = -216.13 kJ mol^{-1}), -COOH functional group (Figure 6C, E_a = -73.09 kJ mol^{-1}), and N-5 functional group (Figure 6E, E_a = -243.01 kJ mol^{-1}) showed extremely high adsorption energy. N-Q improved electrical conductivity and charge transfer ability by enhancing electron transport; C-OH facilitated ion transport efficiency by influencing ion dissolution, and N-6 promoted ion transport by increasing carbon material wettability. These effects collectively reduced Rs to charge/ion transport, enabling electrode materials to achieve high-rate performance and long cycle life in SC. Consequently, the adsorption energy of N-Q/C-OH/N-6 functional groups to K^+ slightly decreased compared to other functional groups. Through the analysis of the results, it can be concluded that several types of N or O species showed unique adsorption capacity, indicating that precise electronic regulation can be achieved at the active site through the synergistic action of O and N species.

Inspired by SHAP analysis of positive feature variables (SSA, -COOH, *etc.*) and structure adsorption sites (N or O doping species), and successful synthesis of ONPC electrode materials, a theoretical adsorption model was established subsequently to evaluate the synergistic effect of multiple physicochemical factors. To simulate a real O, N doped porous carbon surface, the ONPC-900 carbon surface with excellent

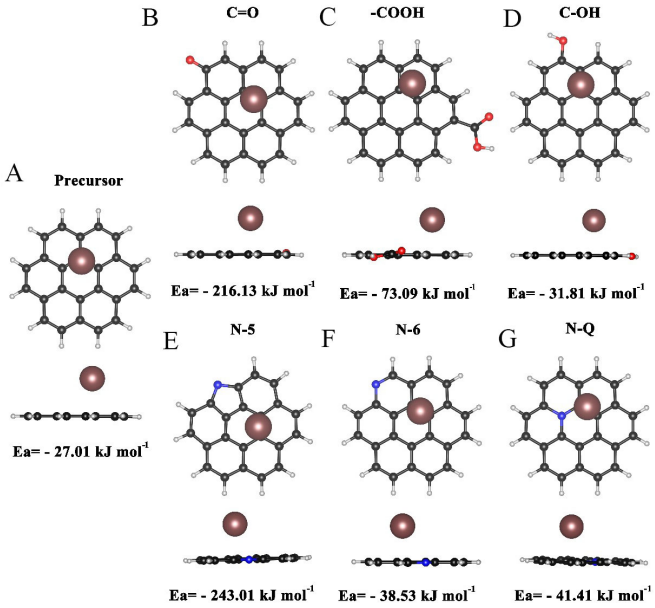

Figure 6. K^+ adsorption on the surface of undoped, O-species and N-species doped carbon. (A) Adsorption of K^+ on an ideal carbon surface (Precursor); (B-D) K^+ adsorption on carbon surfaces doped with different O-doping functional groups; (E-G) Adsorption model of K^+ on doped surfaces with different N functional groups.

performance was chosen for K^+ adsorption based on XPS and pore-size distribution results (mainly distributed in 0.5~0.6 nm, corresponding to the analysis results in Figure 3B, as illustrated in Figure 7. Compared to an ideal carbon model (Figure 7A, E_a = -136.55 kJ mol^{-1}), the adsorption energy of an undoped defect model on the carbon surface (Figure 7B-C, E_a = -401.76 kJ mol^{-1}, E_a = -378.39 kJ mol^{-1}) and O, N co-doped defect model on the carbon surface (ONPC-900, Figure 7D-I) were significantly enhanced. The theoretical calculation of adsorption at different sites showed that O, N inner co-doped configuration [Figure 7G-I] exhibited superior adsorption energies compared to the edge co-doped configuration [Figure 7D-F]. Figure 7I showed the optimal K^+ adsorption energy (E_a = -403.81 kJ mol^{-1}), indicating that the synergistic effects of inner defects (defects attributed to pore formation), N-5, and -COOH active sites promote the adsorption capacity of the electrode to the electrolyte (K^+), thereby improving the electrochemical characteristics of ONPC-900.

Considering the physicochemical properties of ONPC-900 and its excellent electrochemical performance, its practical application in electrode material of supercapacitors was also examined. To explore its application potential at a device level, 6 M KOH as an electrolyte was used to assemble a symmetric supercapacitor (ONPC-900//ONPC-900). Firstly, the CV testing [Figure 8A] of the ONPC-900//ONPC-900 symmetric supercapacitor was recorded at 100 mV s^{-1} and a maximum voltage range varying from 0.8 V to 1.2 V. The CV curves appeared as quasi-rectangular in the voltage window from 0 to 1.0 V, indicating electrochemical stability. Deviations from this shape beyond 1.0 V suggest interactions between the ionic species of the electrolyte and surface functionalities (carbonyl, carboxyl, phenol/benzene hydroxyl, *etc.*) on the carbon electrode. This working voltage range was further confirmed by GCD studies, where the ONPC-900//ONPC-900 symmetric supercapacitor exhibited triangular-shaped curves within the 0-1 V range [Figure 8B], indicative of charge storage through electrical double-layer formation at the electrode/electrolyte interfaces[62]. Substantial deviations from this shape beyond 1 V were observed, leading to an obvious voltage drop. Therefore, all subsequent GCD studies were conducted within the 0-1 V range, consistent with the CV test setting range. Figure 8C illustrated the CV curves of the ONPC-900//ONPC-900

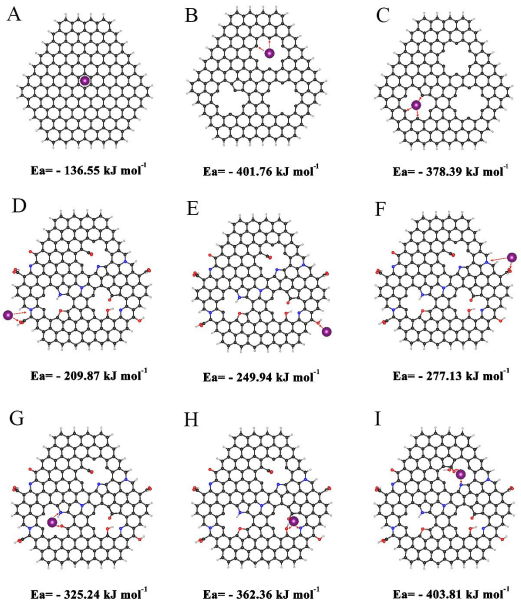

Figure 7. Models of ONPC-900 surface by DFT calculation. The adsorption models for K^+ are (A) on an ideal carbon surface; (B-C) on an undoped defect carbon surface; (D-I) on various O, N co-doped defect carbon surfaces, respectively. ONPC: O, N co-doped hierarchical porous carbon; DFT: Density functional theory.

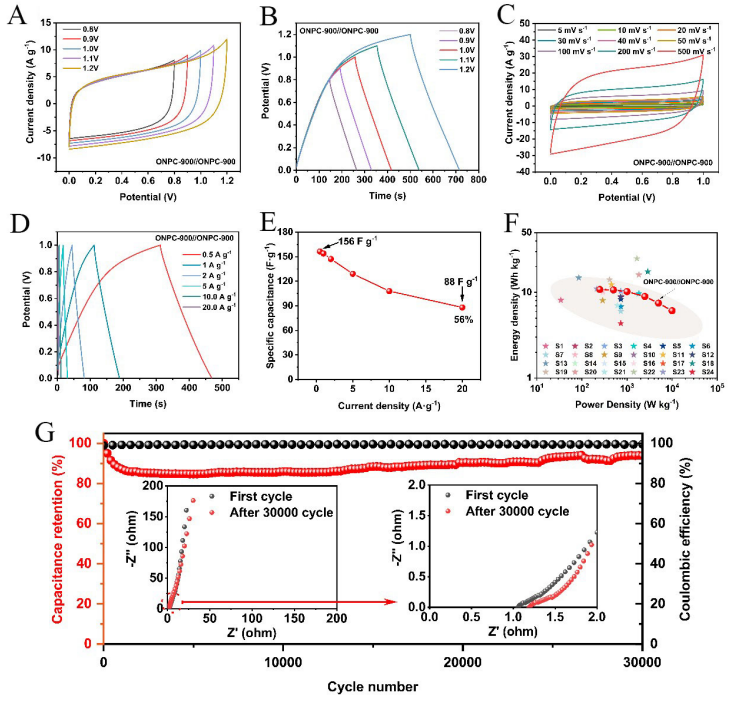

Figure 8. Electrochemical performances of the assembled symmetric supercapacitor by ONPC-900//ONPC-900 in a two-electrode system. (A) CV curves and (B) GCD curves at a scan rate of 100 mV s^{-1} with various current potential windows, respectively; (C) CV curves were measured at various scan rates (5-500 mV s^{-1}); (D) GCD profiles were measured at different current densities (0.5-20 A g^{-1}); (E) SC; (F) Ragone plots, and (G) Cycle life and Coulombic efficiency testing after 30,000 cycles at 5 A g^{-1} in 6.0 mol L^{-1} KOH, inset are the enlarged impedance profile before and after a cyclic stability test. ONPC: O, N co-doped hierarchical porous carbon; CV: Cyclic voltammetry; GCD: Galvanostatic charge-discharge; SC: Specific capacitance.

symmetrical capacitor from 5 to 500 mV s^{-1}, showcasing a quasi-rectangular shape. The GCD curves in Figure 8D, with current densities of 0.5 to 20 A g^{-1}, also exhibited quasi-rectangular and almost symmetric triangle shapes without significant distortion, indicating ideal EDLC capacitive characteristics and confirming excellent electrochemical reversibility. The SC was calculated to be 156 F g^{-1} at 0.5 A g^{-1}, with a capacitance retention exceeding 56% even at a high current density of 20 A g^{-1} [Figure 8E]. The diffusion kinetics of electrolytes in ONPC-900//ONPC-900 symmetrical capacitors was shown in Supplementary Figure 17. The Nyquist diagram of ONPC-900//ONPC-900 symmetrical capacitors displayed characteristic capacitance behaviors, including nearly vertical lines in the low-frequency area, very brief 45° slopes in the intermediate frequency range, and diminutive semicircles within the high-frequency domain [Supplementary Figure 17A], and the phase angle of ONPC-900 is about 82.1°, which is near the phase angle of capacitance (90°) [Supplementary Figure 17B]. The fitted Rs (1.07 Ω) and Rct (0.01 Ω) and the relaxation time (τ0) of 0.66 s [Supplementary Figure 17A and B] indicate the strong conductivity, remarkable charge transfer ability, and rapid ion transport characteristics of the electrolyte in the ONPC-900 electrode. Additionally, the power densities and energy densities of ONPC-900//ONPC-900 symmetrical capacitor were calculated and presented in a Ragone plot [Figure 8F]. The ONPC-900//ONPC-900 symmetrical capacitor demonstrated a maximum energy density of 10.8 Wh kg^{-1} when a power density is 250 W kg^{-1}, and an energy density of 6.1 Wh kg^{-1} corresponding a power density of 10,000 W kg^{-1}, surpassing most previously reported symmetric supercapacitors utilizing coal-derived PCMs or O, N co-doped PCMs in the alkaline electrolyte [Figure 8F, Supplementary Table 8]. The cyclic stability test at a current density of 5 A g^{-1}, as shown in Figure 8G, reveals that the assembled symmetric supercapacitor maintains a high capacitance retention of 93.8% and a CE of 99.7% even after 30,000 cycles, highlighting its excellent electrochemical stability and reversibility. The enhanced stability after 12,000 cycles may be due to the reversible conversion between some N/O doped species in ONPC-900, resulting in increased stability, while CE is widely used to evaluate the reversibility of electrode materials, but because electrochemical tests cannot distinguish between the electrons provided by the main reaction or the side reaction, the CE statistics may be biased. The nearly identical CE throughout the stability test may result from the reversible conversion of N/O-doped species. The magnified Nyquist plots revealed that the slight increase of Rs after 30,000 cycles may be correlated with the morphological and microstructural changes of electrode materials. The overall morphology and element distribution of the ONPC-900 electrodes before and after the test was shown in Supplementary Figure 18A-K. Supplementary Figure 18A and G showed that there is no obvious change in the overall morphology except that the pores between carbon black and ONPC-900 become slightly larger. This may lead to slightly changes in Rs. Elements Mapping of C, N and O were shown in Supplementary Figure 18B-E and Supplementary Figure 18H-K before and after the stability test. The evenly distributed elements of N and O on the C surface further confirm the stability of the ONPC-900 electrode after the long cycle stability test. The relative content of elements shown in Supplementary Figure 18F and L, the slight increase of O content may be related to adsorbed electrolyte (KOH) before and after cyclic stability test. Overall, the ONPC-900//ONPC-900 system displayed exceptional cycle stability and high energy density, affirming its viability for practical carbon-based supercapacitors.

CONCLUSIONS

In summary, SHAP analysis using an emerging ML strategy revealed that the key physicochemical features of SSA and N-5, -COOH functional groups played positive effects in enhancing the capacitance performance in the complex structure-activity relationship. Through ML-assisted interpretability analysis to optimize key features and rational design, the controllable synthesis of ONPC materials was empirically validated via K_2CO_3-assisted pyrolysis, emphasizing the crucial contributions of *in-situ* exfoliation and etching pore generation. Underpinned by this synergistic design, the resulting ONPC-900 with the

synergistic dominant structure retained the amorphous and the graphitized fold features. The hierarchical porous structure of ONPC-900 enriched with abundant sub-nanopores and N-5, -COOH active species, along with high O, N co-doping and graphitization. The analysis of physicochemical features and electrochemical characterization results revealed that the strategic co-doping of N and O within the inner pore defect and high SSA carefully customized the electronic structure of ONPC-900, which promoted ion adsorption and charge transfer and thus promoted the capacitive performance. DFT calculation further confirmed that the synergy of specific N-5, -COOH active sites and internal pore defects functionalized PCMs. Grounded in the adsorption model with synergistic dual-site internal defects, ONPC-900 demonstrated excellent capacitance storage performance. Specifically, the ONPC-900 exhibited a notable SC of 440 F g^{-1} at 0.5 A g^{-1} in a three-electrode system, and symmetric supercapacitors assembled by ONPC-900 demonstrated an exceptional long-term cycle stability of 30,000 cycles and a high-capacity retention rate of 93.8%. Additionally, the material showcased a substantial power density of 250 W kg^{-1} and a maximum energy density of 10.8 Wh kg^{-1}. This work not only underscores the optimal design and controlled synthesis of PCMs with the synergistic structure of double-site and porous defect via regulatory structural engineering, but also improves the capacitive properties of porous carbon. Importantly, an emerging ML and DFT-assisted mechanism interpretation and verification strategy offers new avenues for the integrated structure-activity design of high-performance electrode materials.

DECLARATIONS

Authors' contributions

Conceived the idea and designed the project: Liu, H.; Wang, Y.
Performed data analysis and interpretation: Liu, H.; Cui, Z.; Bai, Q.
Supervised the project: Liu, H.; Cui Z.; Qiao, Z.; Zhang, Y.
Drafted the manuscript: Liu, H.
Revised and finalized the manuscript: Liu, H.; Cui, Z.; Qiao, Z.; Zhang, Y.;, Bai, Q.; Wang, Y.
All authors read and approved the final manuscript.

Availability of data and materials

The data supporting this article have been included as part of the Supplementary Materials.

Financial support and sponsorship

The work was supported by the National Natural Science Foundation of China (No. 52371231), the Key R&D Program of Shanxi Province (No.202302040201008), and the Central Government Guides Local Science and Technology Development Special Fund Projects (No. YDZJSX2022B003).

Conflicts of interest

All authors declared that there are no conflicts of interest.

Ethical approval and consent to participate

Not applicable.

Consent for publication

Not applicable.

REFERENCES

1. Xu, M.; Zhu, X.; Lai, Y.; et al. Production of hierarchical porous biocarbon based on deep eutectic solvent fractionated lignin nanoparticles for high-performance supercapacitor. *Appl. Energy.* **2024**, *353*, 122095. DOI
2. Yang, J.; Su, F.; Liu, T.; Zheng, X. Heteroatoms co-doped multi-level porous carbon as electrode material for supercapacitors with ultra-long cycle life and high energy density. *Diamond. Relat. Mater.* **2024**, *141*, 110693. DOI
3. Sriram, G.; Hegde, G.; Dhanabalan, K.; et al. Recent trends in hierarchical electrode materials in supercapacitor: synthesis, electrochemical measurements, performance and their charge-storage mechanism. *J. Energy. Storage.* **2024**, *94*, 112454. DOI
4. Sharma K, Arora A, Tripathi S. Review of supercapacitors: materials and devices. *J. Energy. Storage.* **2019**, *21*, 801-25. DOI
5. Mansuer, M.; Miao, L.; Qin, Y.; et al. Trapping precursor-level functionalities in hierarchically porous carbons prepared by a pre-stabilization route for superior supercapacitors. *Chinese. Chem. Lett.* **2023**, *34*, 107304. DOI
6. Guo, Z.; Han, X.; Zhang, C.; et al. Activation of biomass-derived porous carbon for supercapacitors: a review. *Chinese. Chem. Lett.* **2024**, *35*, 109007. DOI
7. Jiang, G.; Senthil, R. A.; Sun, Y.; Kumar, T. R.; Pan, J. Recent progress on porous carbon and its derivatives from plants as advanced electrode materials for supercapacitors. *J. Power. Sources.* **2022**, *520*, 230886. DOI
8. Da, S. L. M.; Cesar, R.; Moreira, C. M.; et al. Reviewing the fundamentals of supercapacitors and the difficulties involving the analysis of the electrochemical findings obtained for porous electrode materials. *Energy. Storage. Mater.* **2020**, *27*, 555-90. DOI
9. Yang, N.; Ji, L.; Fu, H.; et al. Hierarchical porous carbon derived from coal-based carbon foam for high-performance supercapacitors. *Chinese. Chem. Lett.* **2022**, *33*, 3961-7. DOI
10. Dong, K.; Sun, Z.; Jing, G.; et al. Nanoarchitectonics of self-supporting porous carbon electrode with heteroatoms co-doped: for high-performance supercapacitors. *J. Energy. Storage.* **2024**, *85*, 111048. DOI
11. Li, H.; Li, Y.; Li, Y.; et al. Facile synthesis of heteroatom-doped hierarchical porous carbon with small mesopores for high-performance supercapacitors. *J. Energy. Storage.* **2024**, *77*, 110000. DOI
12. Yuan, C.; Xu, H.; A El-khodary S, et al. Recent advances and challenges in biomass-derived carbon materials for supercapacitors: a review. *Fuel* **2024**, *362*, 130795. DOI
13. Zhang, R.; Liu, H.; Cui, Z.; Zhang, Y.; Wang, Y. Oxygen-rich microporous carbon derived from humic acid extracted from lignite for high-performance supercapacitors. *Fuel* **2024**, *364*, 131062. DOI
14. Liu, H.; Wang, Y.; Lv, L.; Liu, X.; Wang, Z.; Liu, J. Oxygen-enriched hierarchical porous carbons derived from lignite for high-performance supercapacitors. *Energy* **2023**, *269*, 126707. DOI
15. Peng, Y.; Chen, Z.; Zhang, R.; et al. Oxygen-containing functional groups regulating the carbon/electrolyte interfacial properties toward enhanced K^+ storage. *Nanomicro. Lett.* **2021**, *13*, 192. DOI PubMed PMC
16. Chen, G.; Liu, Z.; Yang, G.; et al. Synthesis of chain-like nitrogen-doped carbon for high-performance supercapacitors. *Colloids. Surf. A:. Physicochem. Eng. Asp.* **2024**, *687*, 133498. DOI
17. Hajibaba, S.; Gholipour, S.; Pourjafarabadi, M.; et al. Electrochemical sulfur-doping as an efficient method for capacitance enhancement in carbon-based supercapacitors. *J. Energy. Storage.* **2024**, *79*, 110044. DOI
18. Suman, S.; Ficek, M.; Sankaran, K. J.; et al. Nitrogen-incorporated boron-doped diamond films for enhanced electrochemical supercapacitor performance. *Energy* **2024**, *294*, 130914. DOI
19. Kim, D.; Jin, X.; Cho, Y.; et al. Facile preparation of N-doped porous carbon nanosheets derived from potassium citrate/melamine for high-performance supercapacitors. *J. Electroanal. Chem.* **2021**, *892*, 115302. DOI
20. Liu, A.; Yan, L.; Zhang, Y.; et al. Nitrogen-doped coal-based microporous carbon material co-activated by HCOOK and urea for high performance supercapacitors. *Surf. Interfaces.* **2024**, *44*, 103754. DOI
21. Farma, R.; Apriyani, I.; Awitdrus; et al. Enhanced electrochemical performance of oxygen, nitrogen, and sulfur trial-doped Nypa fruticans-based carbon nanofiber for high performance supercapacitors. *J. Energy. Storage.* **2023**, *67*, 107611. DOI
22. Zhang, G.; Zhang, Y.; Wang, J.; et al. Nitrogen-functionalization of carbon materials for supercapacitor: Combining with nanostructure directly is superior to doping amorphous element. *J. Colloid. Interface. Sci.* **2024**, *660*, 478-89. DOI
23. Hou, L.; Yang, W.; Li, Y.; et al. Dual-template endowing N, O co-doped hierarchically porous carbon from potassium citrate with high capacitance and rate capability for supercapacitors. *Chem. Eng. J.* **2021**, *417*, 129289. DOI
24. Cai, L.; Zhang, Y.; Ma, R.; et al. Nitrogen-doped hierarchical porous carbon derived from coal for high-performance supercapacitor. *Molecules* **2023**, *28*, 3660. DOI PubMed PMC
25. Zahra, T.; Gassoumi, A.; Gouadria, S.; et al. Facile fabrication of $BiFeO_3$/g-C_3N_4 nanohybrid as efficient electrode materials for supercapacitor application. *Diamond. Relate. Mater.* **2024**, *144*, 110927. DOI
26. Yang, K.; Fan, Q.; Song, C.; et al. Enhanced functional properties of porous carbon materials as high-performance electrode materials for supercapacitors. *Green. Energy. Resour.* **2023**, *1*, 100030. DOI
27. Kolavada, H.; Gajjar, P.; Gupta, S. K. Unraveling quantum capacitance in supercapacitors: energy storage applications. *J. Energy. Storage.* **2024**, *81*, 110354. DOI
28. Shah, S. S.; Aziz, M. A.; Ali, M.; Hakeem, A. S.; Yamani, Z. H. Advanced high-energy all-solid-state hybrid supercapacitor with nickel-cobalt-layered double hydroxide nanoflowers supported on jute stick-derived activated carbon nanosheets. *Small* **2024**, *20*, e2306665. DOI PubMed
29. Reddy, B.; Narayana, P.; Maurya, A.; et al. Modeling capacitance of carbon-based supercapacitors by artificial neural networks. *J. Energy. Storage.* **2023**, *72*, 108537. DOI

30. Liu, P.; Wen, Y.; Huang, L.; et al. An emerging machine learning strategy for the assisted□design of high-performance supercapacitor materials by mining the relationship between capacitance and structural features of porous carbon. *J. Electroanal. Chem.* **2021**, *899*, 115684. DOI
31. Rahimi, M.; Abbaspour-fard, M. H.; Rohani, A. Synergetic effect of N/O functional groups and microstructures of activated carbon on supercapacitor performance by machine learning. *J. Power. Sources.* **2022**, *521*, 230968. DOI
32. Saad, A. G.; Emad-eldeen, A.; Tawfik, W. Z.; El-deen, A. G. Data-driven machine learning approach for predicting the capacitance of graphene-based supercapacitor electrodes. *J. Energy. Storage.* **2022**, *55*, 105411. DOI
33. Krishnan, A.; Yoosuf, M.; Archana, K.; A s. A, Viswam A. Metal derivative (MD)/g-C_3N_4 association in hydrogen production: a study on the fascinating chemistry behind, current trend and future direction. *J. Energy. Chem.* **2023**, *80*, 562-83. DOI
34. Kresse, G.; Furthmüller, J. Efficient iterative schemes for ab initio total-energy calculations using a plane-wave basis set. *Phys. Rev. B. Condens. Matter.* **1996**, *54*, 11169-86. DOI PubMed
35. Jha, S.; Yen, M.; Salinas, Y. S.; Palmer, E.; Villafuerte, J.; Liang, H. Machine learning-assisted materials development and device management in batteries and supercapacitors: performance comparison and challenges. *J. Mater. Chem. A.* **2023**, *11*, 3904-36. DOI
36. Qiu, C.; Jiang, L.; Gao, Y.; Sheng, L. Effects of oxygen-containing functional groups on carbon materials in supercapacitors: a review. *Mater. Des.* **2023**, *230*, 111952. DOI
37. Thi, Q. H.; Man, P.; Huang, L.; Chen, X.; Zhao, J.; Ly, T. H. Superhydrophilic 2D carbon nitrides prepared by direct chemical vapor deposition. *Small. Sci.* **2023**, *3*, 2200099. DOI
38. Yang, H.; Lin, H.; Yang, C.; et al. Structural regulation of carbon materials through hydrothermal mixing of biomass and its application in supercapacitors. *J. Energy. Storage.* **2024**, *83*, 110688. DOI
39. Yang, B.; Zhang, D.; Li, Y.; et al. Locally graphitized biomass-derived porous carbon nanosheets with encapsulated Fe_3O_4 nanoparticles for supercapacitor applications. *Chem. Eng. J.* **2024**, *479*, 147662. DOI
40. Ran, F.; Yang, X.; Xu, X.; Li, S.; Liu, Y.; Shao, L. Green activation of sustainable resources to synthesize nitrogen-doped oxygen-riched porous carbon nanosheets towards high-performance supercapacitor. *Chem. Eng. J.* **2021**, *412*, 128673. DOI
41. Liu, Z.; Qin, A.; Zhang, K.; Lian, P.; Yin, X.; Tan, H. Design and structure of nitrogen and oxygen co-doped carbon spheres with wrinkled nanocages as active material for supercapacitor application. *Nano. Energy.* **2021**, *90*, 106540. DOI
42. Raha, H.; Pradhan, D.; Guha, P. K. Ultrahigh coulombic efficiency in alkali metal incorporated biomass derived carbon electrode. *J. Electroanal. Chem.* **2023**, *931*, 117193. DOI
43. Song, Z.; Li, L.; Zhu, D.; et al. Synergistic design of a N, O co-doped honeycomb carbon electrode and an ionogel electrolyte enabling all-solid-state supercapacitors with an ultrahigh energy density. *J. Mater. Chem. A.* **2019**, *7*, 816-26. DOI
44. Le, F.; Ren, P.; Jia, W.; Wang, T.; Tao, Y.; Wu, D. High-yield preparation of coal tar pitch based porous carbon via low melting point fire retardant carbonation strategy for supercapacitor. *Chem. Eng. J.* **2023**, *470*, 144131. DOI
45. Yang, Y.; Zuo, P.; Qu, S. Adjusting hydrophily and aromaticity strategy for pitch-based hierarchical porous carbon and its application in flexible supercapacitor. *Fuel* **2022**, *311*, 122514. DOI
46. Zhang, H.; Sun, X.; Zheng, Y.; Zhou, J. Scalable synthesis of N, O co-doped hierarchical porous carbon for high energy density supercapacitors. *J. Colloid. Interface. Sci.* **2024**, *658*, 1025-34. DOI
47. Li, W.; Li, C.; Xu, Y.; et al. Heteroatom-doped and graphitization-enhanced lignin-derived hierarchically porous carbon via facile assembly of lignin-Fe coordination for high-voltage symmetric supercapacitors. *J. Colloid. Interface. Sci.* **2024**, *659*, 374-84. DOI
48. Zhang, Y.; Zheng, H.; Wang, Q.; et al. 3-Dimensional porous carbon derived from waste aucklandia lappa straw for high-performance liquid and all-solid-state supercapacitors. *J. Electroanal. Chem.* **2024**, *953*, 117992. DOI
49. Zheng, L.; Dai, X.; Ouyang, Y.; Chen, Y.; Wang, X. nHighly N/O co-doped carbon nanospheres for symmetric supercapacitors application with high specific energy. *J. Energy. Storage.* **2021**, *33*, 102152. DOI
50. Ma, T.; Xu, S.; Zhu, M. Porous carbon from verbena straw with self-doped O/N and its high-performance aqueous and flexible all-solid-state supercapacitors. *J. Power. Sources.* **2024**, *597*, 234147. DOI
51. Shaku, B.; Mofokeng, T.; Coville, N.; Ozoemena, K.; Maubane-nkadimeng, M. Biomass valorisation of marula nutshell waste into nitrogen-doped activated carbon for use in high performance supercapacitors. *Electrochim. Acta.* **2023**, *442*, 141828. DOI
52. Feng, L.; Wang, M.; Chang, Y.; et al. Polymerization-Pyrolysis-Derived Hierarchical Nitrogen-Doped Porous Carbon for Energetic Capacitive Energy Storage. *ACS. Appl. Energy. Mater.* **2023**, *6*, 7147-55. DOI
53. Wang, T.; Guo, J.; Guo, Y.; Feng, J.; Wu, D. Nitrogen-Doped Carbon Derived from Deep Eutectic Solvent as a High-Performance Supercapacitor. *ACS. Appl. Energy. Mater.* **2021**, *4*, 2190-200. DOI
54. Dong, D.; Zhang, Y.; Xiao, Y.; Wang, T.; Wang, J.; Gao, W. Oxygen-enriched coal-based porous carbon under plasma-assisted $MgCO_3$ activation as supercapacitor electrodes. *Fuel* **2022**, *309*, 122168. DOI
55. Zhang, Z.; Li, Y.; Yang, X.; et al. In-situ confined construction of N-doped compact bamboo charcoal composites for supercapacitors. *J. Energy. Storage.* **2023**, *62*, 106954. DOI
56. Park, S.; Seo, B.; Shin, D.; Kim, K.; Choi, W. Sodium-chloride-assisted synthesis of nitrogen-doped porous carbon shells via one-step combustion waves for supercapacitor electrodes. *Chem. Eng. J.* **2022**, *433*, 134486. DOI
57. Li, G.; Chen, S.; Wang, Y.; Wang, G.; Wu, Y.; Xu, Y. N, S co-doped porous graphene-like carbon synthesized by a facile coal tar pitch-blowing strategy for high-performance supercapacitors. *Chem. Phys. Lett.* **2023**, *827*, 140712. DOI
58. Yang, X.; Sun, G.; Wang, F.; et al. Rational design of dense microporous carbon derived from coal tar pitch towards high mass loading supercapacitors. *J. Colloid. Interface. Sci.* **2023**, *646*, 228-37. DOI

59. Dong, D.; Zhang, Y.; Xiao, Y.; et al. High performance aqueous supercapacitor based on nitrogen-doped coal-based activated carbon electrode materials. *J. Colloid. Interface. Sci.* **2020**, *580*, 77-87. DOI
60. Dong, D.; Xiao, Y.; Xing, J. Facile wet mechanochemistry coupled K_2FeO_4 activation to prepare functional coal-derived hierarchical porous carbon for supercapacitors. *J. Cleaner. Prod.* **2023**, *428*, 139474. DOI
61. Zhang, R.; Jing, X.; Chu, Y.; et al. Nitrogen/oxygen co-doped monolithic carbon electrodes derived from melamine foam for high-performance supercapacitors. *J. Mater. Chem. A.* **2018**, *6*, 17730-9. DOI
62. Yadav, N.; Singh, M. K.; Yadav, N.; Hashmi, S. High performance quasi-solid-state supercapacitors with peanut-shell-derived porous carbon. *J. Power. Sources.* **2018**, *402*, 133-46. DOI